Visualization of Chromatin Decompaction and Break Site Extrusion as Predicted by Statistical Polymer Modeling of Single-Locus Trajectories

Citation: Amitai, Assaf; Seeber, Andrew; Gasser, Susan M. and Holcman, David. "Visualization of Chromatin Decompaction and Break Site Extrusion as Predicted by Statistical Polymer Modeling of Single-Locus Trajectories." Cell Reports 18, no. 5 (January 2017): 1200–1214 © 2017 The Author(s)

As Published: http://dx.doi.org/10.1016/j.celrep.2017.01.018

Publisher: 2211-1247

Persistent URL: http://hdl.handle.net/1721.1/109829

Version: Final published version: final published article, as it appeared in a journal, conference proceedings, or other formally published context

Article

Cell Reports

Visualization of Chromatin Decompaction and Break Site Extrusion as Predicted by Statistical Polymer Modeling of Single-Locus Trajectories

Graphical Abstract

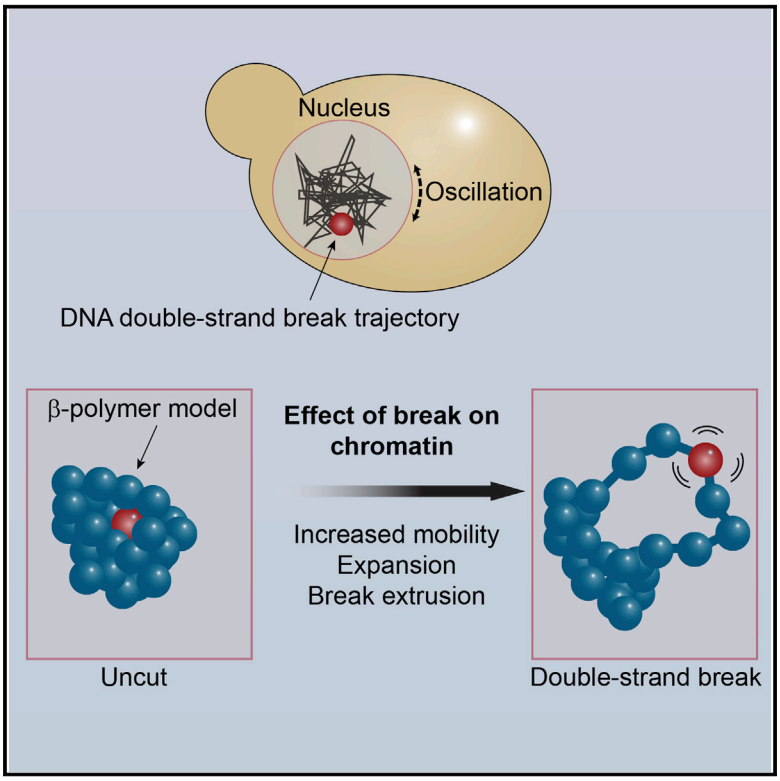

Authors

Assaf Amitai, Andrew Seeber, Susan M. Gasser, David Holcman

Correspondence

susan.gasser@fmi.ch (S.M.G.), david.holcman@ens.fr (D.H.)

In Brief

Amitai et al. present a robust analytical workflow for the analysis of single-particle trajectories. The extracted biophysical parameters allow accurate modeling of chromatin dynamics. The authors predict and show that, at double-strand breaks, chromatin decompacts and induces break relocation, while nuclear oscillation arises from cytoskeleton forces.

Highlights

- A robust analytical workflow for single-particle trajectories is presented
- β-polymer modeling predicts chromatin expansion at double-strand breaks
- Altered nucleosome interaction drives break extrusion from a chromatin domain
- Effects of local chromatin are distinct from actin-driven nuclear oscillation

Amitai et al., 2017, Cell Reports *18*, 1200–1214
January 31, 2017
http://dx.doi.org/10.1016/j.celrep.2017.01.018

CellPress

OPEN ACCESS
CellPress

Cell Reports
Article

Visualization of Chromatin Decompaction and Break Site Extrusion as Predicted by Statistical Polymer Modeling of Single-Locus Trajectories

Assaf Amitai,[1,2,6] Andrew Seeber,[3,4,6] Susan M. Gasser,[3,4,7,*] and David Holcman[1,5,*]
[1]Institut de Biologie de l'École Normale Supérieure, Ecole Normale Supérieure, 46 rue d'Ulm, 75005 Paris, France
[2]Institute for Medical Engineering & Science, Massachusetts Institute of Technology, Cambridge, MA 02139, USA
[3]Friedrich Miescher Institute for Biomedical Research, Maulbeerstrasse 66, 4058 Basel, Switzerland
[4]Faculty of Natural Sciences, University of Basel, 4056 Basel, Switzerland
[5]Department of Applied Mathematics and Theoretical Physics, University of Cambridge and Churchill College, Cambridge CB30DS, UK
[6]Co-first author
[7]Lead Contact
*Correspondence: susan.gasser@fmi.ch (S.M.G.), david.holcman@ens.fr (D.H.)
http://dx.doi.org/10.1016/j.celrep.2017.01.018

SUMMARY

Chromatin moves with subdiffusive and spatially constrained dynamics within the cell nucleus. Here, we use single-locus tracking by time-lapse fluorescence microscopy to uncover information regarding the forces that influence chromatin movement following the induction of a persistent DNA double-strand break (DSB). Using improved time-lapse imaging regimens, we monitor trajectories of tagged DNA loci at a high temporal resolution, which allows us to extract biophysical parameters through robust statistical analysis. Polymer modeling based on these parameters predicts chromatin domain expansion near a DSB and damage extrusion from the domain. Both phenomena are confirmed by live imaging in budding yeast. Calculation of the anomalous exponent of locus movement allows us to differentiate forces imposed on the nucleus through the actin cytoskeleton from those that arise from INO80 remodeler-dependent changes in nucleosome organization. Our analytical approach can be applied to high-density single-locus trajectories obtained in any cell type.

INTRODUCTION

Ever since the first live imaging of chromatin dynamics by single-particle tracking (Marshall et al., 1997), much effort has been invested into understanding the regulation and biological function of DNA movement. Unlike the directional separation of sister chromatids in mitosis, the interphase movement of chromatin is stochastic, yet it is modulated by ATP levels, suggesting that DNA dynamics are influenced by enzymatic events (Heun et al., 2001; Levi et al., 2005; Marshall et al., 1997; Seeber et al., 2013). Indeed, the majority of chromatin movement monitored in eukaryotic nuclei is subdiffusive (Albert et al., 2013; Amitai et al., 2015; Dion and Gasser, 2013; Weber et al., 2012), being restricted to volumes significantly smaller than that of the nucleus, arguing that internal forces constrain chromatin movement (Gartenberg et al., 2004; Bystricky, 2015; Chubb et al., 2002; Marshall, 2002). In budding yeast, such constraint has been altered by either the ablation of sister chromatid cohesion (Dion et al., 2013), the targeting of nucleosome remodelers (Neumann et al., 2012), or the elimination of anchorage sites that tether yeast chromosomes to nuclear substructures, such as the inner nuclear membrane protein Esc1 (Gartenberg et al., 2004), nuclear pores (Horigome et al., 2014), or the spindle pole body (Strecker et al., 2016; Verdaasdonk et al., 2013).

Chromatin movement is thought to facilitate gene induction by allowing distant enhancers and promoters to interact (Amitai and Holcman, 2013a; Bell and Felsenfeld, 1999; Dillon et al., 1997; Ptashne, 1986) or to facilitate the long-range search for sequence homology during DNA double-strand break repair (Agmon et al., 2013; Dion and Gasser, 2013; Miné-Hattab and Rothstein, 2012). More generally, the accessibility of DNA sequence for recognition by either proteins or nucleic acid may benefit from chromatin mobility. As an example, a fluorescently tagged locus with a persistent double-strand break (DSB) in budding yeast, shows greater movement than the same locus undamaged (Dion et al., 2012; Miné-Hattab and Rothstein, 2012). The drivers of this increased mobility and their impact on repair are debated (Dion et al., 2012; Miné-Hattab and Rothstein, 2012; Strecker et al., 2016; Verdaasdonk et al., 2013), yet the fact that increased movement depends on the type of damage incurred (Dion et al., 2012, 2013) and on a kinase-mediated DNA damage checkpoint response (Miné-Hattab and Rothstein, 2012; Seeber et al., 2013; Strecker et al., 2016) argues for physiological relevance.

In mammals as well, the chromatin context of a DSB and the preference of the locus for repair by end joining or ectopic recombination influence whether or not a locus will show enhanced movement following damage induction (Aten et al., 2004; Cho et al., 2014; Jakob et al., 2009; Krawczyk et al., 2012; Kruhlak et al., 2006; Lottersberger et al., 2015; Nelms et al., 1998; Roukos et al., 2013; Soutoglou et al., 2007; Tsouroula et al., 2016).

Radiation-induced foci and uncapped telomeres both show enhanced movement in mammalian cells (Dimitrova et al., 2008; Lottersberger et al., 2015), and in both mammals and flies it was shown that DSBs that occur in heterochromatin must move out of the heterochromatic compartment in order to be repaired by recombination (Chiolo et al., 2011; Jakob et al., 2011; Ryu et al., 2015; Tsouroula et al., 2016). What changes occur on a biophysical level to allow such movements are unclear, but possible triggers could be changes in local chromatin structure, the release of constraints imposed by non-chromatin anchorage sites, or active, motor-driven transport.

To date, the analysis applied to single-particle trajectories (SPTs) of tagged chromatin loci has been inadequate to distinguish between these possibilities. Here, we present a framework for statistical analysis of SPTs over time that allows us to extract a more comprehensive set of biophysical parameters and relate them to polymer models (Amitai and Holcman, 2013b; Amitai et al., 2015). We then use simulations based on the β-polymer model to predict chromatin behavior. Our experimental system is the well-characterized HO endonuclease- induced DSB in budding yeast (Dion et al., 2012; Horigome et al., 2014; Miné-Hattab and Rothstein, 2012; Nagai et al., 2008), which allows us to monitor locus dynamics before and after DSB induction. Polymer modeling predicts that chromatin around a break will expand and that this will drive extrusion of the damage from its local chromatin domain. We confirm chromatin expansion at an induced DSB using quantitative, super-resolution structured illumination microscopy (SIM). Moreover, we demonstrate a significant increase in the anomalous exponent of movement, α, at a DSB in the rDNA, as it shifts from the nucleolus for recombination-mediated repair (Torres-Rosell et al., 2007).

Our approach consists of two parts. First, we extract from single-locus trajectories an ensemble of four statistical parameters derived from polymer model analysis. These parameters provide independent information about the nature of locus movement, allowing us to characterize the origin of the forces acting on chromatin. We then construct a polymer model and simulate chromatin behavior, using empirically extracted biophysical parameters. This analytical approach and predictive modeling enable a biophysical definition of chromatin dynamics and provide a paradigm for the analysis of chromatin movement in other species. In yeast, we show that changes in local chromatin structure at a break can lead to altered dynamics that can affect longer-range aspects of chromatin organization.

RESULTS

We use a well-characterized budding yeast strain carrying a galactose-inducible *HO* gene, which encodes the Homothallic switching endonuclease that, in turn, introduces a double-strand break specifically and uniquely at the *MAT* locus on Chr III (Table S1). Cleavage efficiency is measured for each experiment by qPCR (Table S2). We visualize the locus by tracking a fluorescent LacI-GFP protein bound to an array of *lac* operators (*lacO*) that is inserted near the cut site (Figure 1A). In addition, we have tagged the nuclear pores with a separate red fluorophore (Nup49-Ruby2), which is both brighter than traditional fluorophores and more photostable (Lee et al., 2013). This allows us to use less light to stimulate the fluorochrome, minimizing light-induced damage despite longer acquisition times. Our imaging regimens do not activate the DNA damage response and cells continue to divide after light exposure (Figure S1). The labeling of the nuclear perimeter with Nup49-Ruby2 allows us to align acquired trajectories with respect to the nuclear center, to correct for translational movement.

Previous studies of chromatin dynamics performed SPTs with imaging intervals of 1.5 s for 200 frames (Dion et al., 2012; Neumann et al., 2012; Strecker et al., 2016), 10 s for 80 frames (Miné-Hattab and Rothstein, 2012), 30 s for 20 frames (Verdaasdonk et al., 2013), 100 ms for 300 frames (Spichal et al., 2016), and 15–400 ms for 300 frames (Hajjoul et al., 2013). Without sufficient time points, statistically significant information cannot always be extracted from SPTs. In addition, chromatin motion may show different properties when imaged at different timescales (Amitai et al., 2015; Hajjoul et al., 2013; Levi et al., 2005). We addressed these caveats by acquiring 3D images at two timescales and generating more frames than had previously been published. Namely, 750 or 500 3D stacks of images were obtained for each time-lapse movie at Δt = 80 ms (10 ms per z-slice ×8) or Δt = 300 ms (30 ms per z-slice ×8), respectively (Figure 1A). By selecting a small cropped region on the EM-CCD chip and synchronizing the Piezo z-stage, we could stream acquisitions just above the camera chip readout rate (~9 ms). We simultaneously captured the two fluorophores, i.e., the LacI-GFP at *MAT* and the perinuclear Nup49-Ruby2, and by coupling a EM-CCD camera with 3D deconvolution by Huygens Professional, we could use very-low-light conditions over extended periods of capture. It is important to note that DNA shows significantly less movement in S-phase yeast cells than in G1-phase cells (Dion et al., 2013; Heun et al., 2001); thus, reliable data cannot be extracted from tracking a field of asynchronous yeast cells. Single cells must be selected and the data triaged after determining the cell-cycle stage of each imaged cell. In this study, we selected only small budded S-phase cells for spot tracking.

To extract information from these SPTs we introduce four statistical quantities that can be computed from the data (numerical code to compute the four parameters is accessible at http://bionewmetrics.org/ in the "Nuclear Organization section"). For clarity, and to make this method accessible to a general audience, the majority of the equations defining these parameters are in the Supplemental Information. Their extraction is key to our analysis, because these parameters provide independent, complementary information on first- and second-moment statistics. Each has been studied separately elsewhere and are described below.

1. The length of constraint L_C is defined as the SD of the locus position with respect to its mean averaged over time. This parameter provides estimation for the apparent radius of the volume explored by a finite trajectory. For a trajectory containing N_p points, where $\mathbf{R}_c(k\Delta t)$ is the position of a locus at a time t, L_C is obtained from the empirical estimation:

$$L_C = \sqrt{\mathrm{Var}(\mathbf{R}_c)} \approx \sqrt{\frac{1}{N_p}\sum_{k=1}^{N_p}(\mathbf{R}_c(k\Delta t) - \langle \mathbf{R}_c \rangle)^2}. \quad \text{(Equation 1)}$$

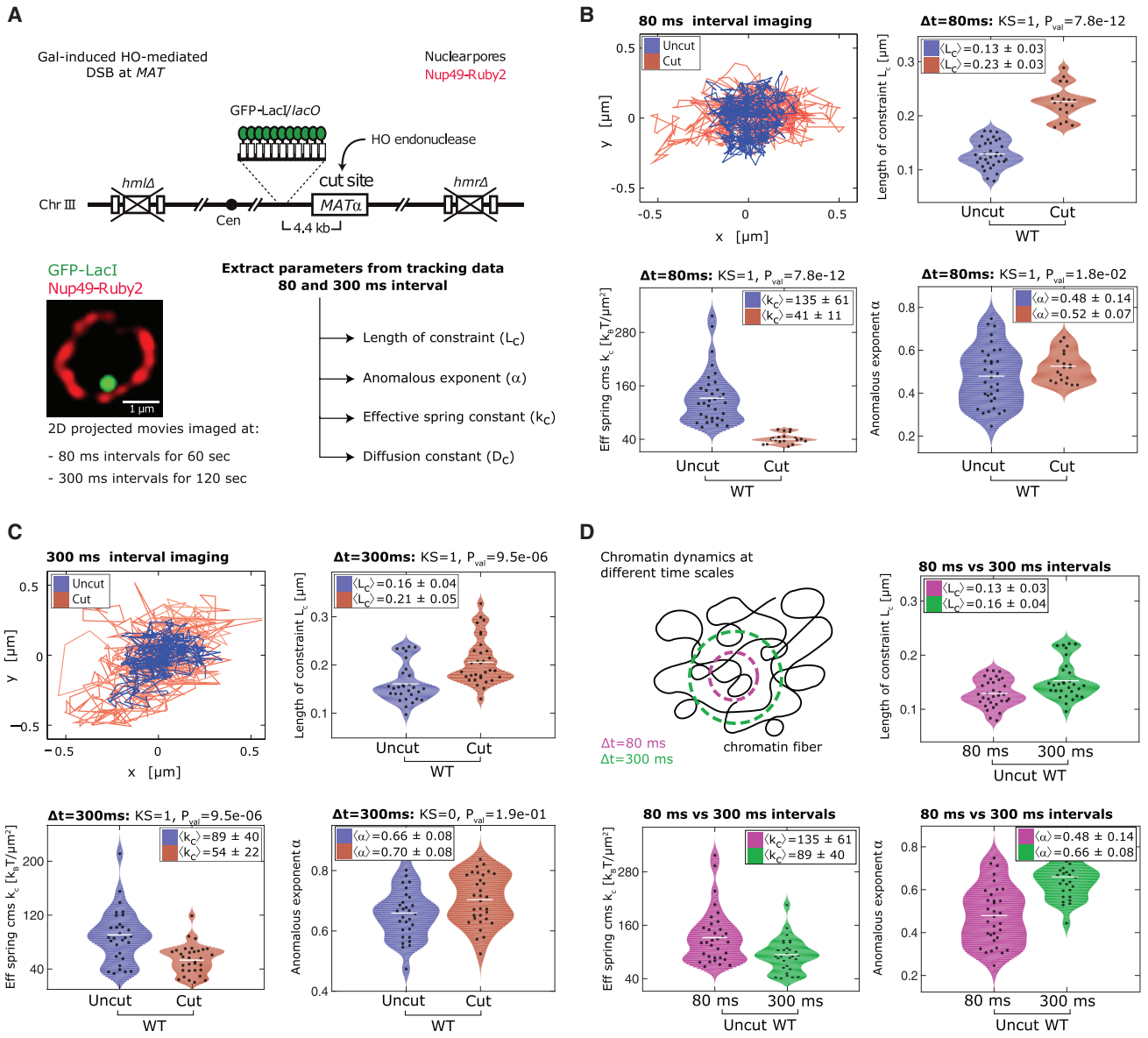

Figure 1. Extraction of Biophysical Parameters of DSB Dynamics Using Two Imaging Regimens

(A) Schematics of the experimental system and description of extracted biophysical parameters. See text and Supplemental Information for definition of length of constraint (Lc), effective spring coefficient (k_c), the anomalous exponent α reflecting an auto-correlation function, and the D_c (diffusion coefficient).

(B) Upper-left quadrant: *MAT* locus trajectories during 60 s (Δt = 80 ms). Other quadrants contain the extracted parameters Lc, kc, and α of cut (red) and uncut (blue) *MAT* loci. Above the panel, the p value of a Kolmogorov-Smirnov (KS) test is indicated. White bar, distribution mean. Strains used are GA-8862/8863 (Table S1).

(C) As in (B) but for Δt = 300 ms during 120 s. For extracted parameters, see Table 1 and Figure S2. Cut efficiencies and nuclei scored are in Table S2.

(D) Monitoring movement at different timescales corresponds to studying the polymer on different scales. The time resolution determines the scale of chromatin dynamics monitored; at a short time resolution (80 ms, pink circle), we observed a smaller element of the chromatin movement than with 300 ms resolution (green circle). Panels present parameters Lc, kc, and α from 80- and 300-ms imaging regimens for an intact locus (see Figures S1 and S2).

It characterizes the confinement of a locus, which in other studies has been reported as the radius of confinement (R_{conf} – not to be confused with R_c). The R_{conf} is computed from the asymptotic plateau of mean square displacement (MSD) curves and is therefore limited to trajectories that plateau. This is strongly influenced by the length of image acquisition. The advantage of computing L_C is that it gives a robust estimate of the volume $V = 4/3\pi L_C^3$ occupied by the trajectory and can be used on any kind of trajectory, as it does not require a plateau (see Supplemental Information).

2. The anomalous exponent α is computed from the auto-correlation (AC, Supplemental Information Equation 11) function for small increments $\boldsymbol{C}(t) = \langle(\mathbf{R_c}(\tau+t) - \mathbf{R_c}(\tau))^2\rangle \approx t^{\alpha}$. It indicates the nature of the locus motion; i.e., α = 1 describes normal diffusion, while

Table 1. Biophysical Parameters Extracted from SPTs before and after DSB Induction

Description	Parameters	Uncut Locus	Cut Locus
Δt = 80 ms			
Length of constraint	L_C	0.13 ± 0.03μm	0.23 ± 0.03μm
Anomalous exponent	α	0.49 ± 0.14	0.52 ± 0.07
Effective spring coefficient	k_c	139 ± 63k_BT/μm^2	41 ± 11k_BT/μm^2
Apparent diffusion constant	D_c	14.3 ± 7.5 × 10^{-3}μm^2/s	27.8 ± 10.8 × 10^{-3}μm^2/s
Δt = 300 ms			
Length of constraint	L_C	0.16 ± 0.04μm	0.21 ± 0.05μm
Anomalous exponent	α	0.66 ± 0.08	0.70 ± 0.08
Effective spring coefficient	k_c	89 ± 40k_BT/μm^2	54 ± 22k_BT/μm^2
Apparent diffusion constant	D_c	3.9 ± 1.1 × 10^{-3}μm^2/s	3.9 ± 1.6 × 10^{-3}μm^2/s

Yeast strains, conditions of imaging, and cut induction are as in Figures 1B and 1C.

$\alpha < 1$ is subdiffusive (constrained) and $\alpha > 1$ is superdiffusive (directed) movement (Kepten et al., 2013; Dion and Gasser, 2013). In practice, we estimated α by fitting the first six points of the AC function of an SPT by a power law t^{α}, as described in the Supplemental Information. Every time point affects the initial slope of the AC function (or the MSD); thus, movies with more time points will ultimately provide the more accurate approximation of α, and a more robust representation of the data.

3. The effective spring coefficient k_c. An external force acting on a chromatin locus can be modeled as a spring force applied on a single monomer belonging to a polymer. This force affects the entire polymer motion and can be recovered from the first-order moment statistics of single-locus trajectories. The spring force acting at position x_a and measured at position x_m is represented by $F = -k_c (x_m - x_a)$, and the spring constant k_c allows us to estimate the effect of local tethering interactions around the locus of interest (Amitai et al., 2015) (see Supplemental Information, Equation 17). This tethering can arise from interactions of the locus with other chromosomes or nuclear substructures, such as the nucleolus or nuclear envelope. While these interactions cannot be measured directly they can be inferred from SPTs.
4. The effective diffusion coefficient D_c reflects the second-order statistical properties of a trajectory. This diffusion coefficient accounts for local crowding that may vary along the trajectory. The estimation procedure is described in the Supplemental Information.

These four parameters are complementary (monitoring first- and second-order moment statistics) and provide an advantage over those extracted previously, which were generally limited to determination of the radius of confinement (R_{conf}) and/or the diffusion coefficient. We use them to characterize the underlying motion of the monitored locus. In summary, the confinement of a locus is measured by L_C, its velocity is D_c, forces acting on a locus is given by k_c, and, importantly, the nature of the motion is described by α.

Induction of a DSB Alters the Biophysical Parameters of a Chromatin Locus

Consistent with previous results that monitored the dynamics of induced DSBs in yeast (Dion et al., 2012; Miné-Hattab and Rothstein, 2012), we find that Lc increases significantly after break induction in both timescales from $L_c^{uncut\ 80ms}$ = 0.13 ± 0.03 μm to $L_c^{cut\ 80ms}$ = 0.23 ± 0.03 μm and $L_c^{uncut\ 300ms}$ = 0.16 ± 0.04 μm to $L_c^{cut\ 300ms}$ = 0.21 ± 0.05 μm (Figures 1B and 1C, summarized in Table 1). Comparing the Lc values for unbroken loci tracked at Δt = 80- versus 300-ms intervals, we find that the 300-ms trajectories have a higher L_C. The 300 ms-interval movies are 120 s long and the 80-ms movies are 60 s long, consistent with the notion that Lc scales with the time during which the locus has explored its surroundings.

The increase in movement upon break induction could reflect the loss of constraint (either from reduced contacts between nucleosomes or reduced interaction with a less mobile nuclear substructure), or stem from an increased external force acting on the nucleus. Yeast chromosomes reversibly interact with nuclear envelope structures (e.g., pores or the spindle pole body [SPB] (Taddei and Gasser, 2012). Such interactions not only constrain movement, but could enhance it, if the nucleus experiences forces leading to rotation or oscillation. To quantify the strength of tethering interactions at the site of a DSB, we approximate the confining tethering force using the classical harmonic potential approximation (Amitai et al., 2015). A binding force is generically parabolic (see Supplemental Information); thus, a tethering force is characterized by a strength k acting on a single monomer R_n: $U = (1/2)k(\mathbf{R}_n - \boldsymbol{\mu})^2$, where μ is the position of the interaction. Reduction of tethering forces should result in increased mobility (Amitai et al., 2015). Based on these modeling predictions, we extracted the effective spring coefficient k_c (Equation 17, Supplemental Information), which measures the averaged external forces affecting the observed locus. We find that k_c decreases significantly for both timescales from $k_c^{uncut\ 80ms}$ = 135 ± 61 k_BT/μm^2 to $k_c^{cut\ 80ms}$ = 41 ± 11 k_BT/μm^2 and $k_c^{uncut\ 300ms}$ = 89 ± 40 k_BT/μm^2 to $k_c^{cut\ 300ms}$ = 54 ± 22 k_BT/μm^2 (Figures 1B and 1C). This decay suggests that there is a local reduction in interactions around the region of the break. This could increase

the territory the spot explores, as reflected in the increase of the length L_C.

Upon cut induction, we also find a small but significant increase in the anomalous exponent α where $\alpha^{uncut\ 80ms} = 0.48 \pm 0.14$ increases to $\alpha^{cut\ 80ms} = 0.52 \pm 0.07$ and $\alpha^{uncut\ 300ms} = 0.66 \pm 0.08$ increases to $\alpha^{cut\ 300ms} = 0.70 \pm 0.08$ (Figures 1B and 1C). Surprisingly, we found that the anomalous exponent α is consistently higher at $\Delta t = 300$ ms ($\alpha^{uncut\ 80ms} = 0.48$ versus $\alpha^{uncut\ 300ms} = 0.66$), even without DSB induction. This difference could arise from the fact that by choosing a time step we implicitly establish a cutoff below which locus dynamics are no longer influenced by the long-range chromatin properties. Vice versa, at larger intervals (e.g., $\Delta t = 300$ ms), the more subtle changes in chromatin dynamics that occur on shorter timescales ($\Delta t = 80$ ms) may be averaged out (see scheme, Figure 1D). Thus, rapid image acquisition allows us to observe fluctuations of polymer structure at the level of short genomic distances, while larger time intervals reveals local fluctuations of chromatin at larger genomic scales. This also provides an explanation of why we observe an increase in the diffusion coefficient after cleavage for the trajectories at $\Delta t = 80$ ms ($D_c^{Uncut\ 80ms} = 15.4 \pm 7.7 \times 10^{-3}\ \mu m^2/s$ to $D_c^{cut\ 80ms} = 27.8 \pm 10.8 \times 10^{-3}\ \mu m^2/s$), but not at $\Delta t = 300$ ms ($D_c^{Uncut\ 300ms} = 3.9 \pm 1.1 \times 10^{-3}\ \mu m^2/s$ versus $D_c^{cut\ 300ms} = 3.9 \pm 1.6 \times 10^{-3}\ \mu m^2/s$; Equation 13, Supplemental Information; Figure S2, Table 1).

Effect of Actin Depolymerization on Chromatin Dynamics

Since the increase in the anomalous exponent α upon DSB induction was small ($\alpha^{uncut\ 80ms} = 0.46$ versus $\alpha^{cut\ 80ms} = 0.52$) and because α increased with longer imaging intervals, we hypothesized that external forces might act on the nucleus that could mask changes in α. While our tracking regimen corrects for translational movement, it cannot account for nuclear rotation or precession. As a simple proof of principle that α increases when an oscillating force is applied to the polymer, we simulated a Rouse polymer ($\alpha = 0.5$) with oscillation period ω (Supplemental Information; Figure S3). We find that when $\omega = 0.04$, α increases from 0.5 to 0.7 (Figure 2A), suggesting that nuclear rotation/precession would increase α and could, therefore, mask changes in this parameter. This simulation was performed for a Rouse polymer, yet simulation of other polymer models would yield the same qualitative behavior.

Next, we tested whether this effect occurs in vivo. Recent work has implicated the cytoskeleton (Lottersberger et al., 2015; Spichal et al., 2016) and KASH proteins, which anchor inner nuclear membrane-spanning SUN domain proteins to the cytoskeleton (Starr and Fridolfsson, 2010) in chromatin movement (Chung et al., 2015; Lottersberger et al., 2015; Spichal et al., 2016). Given that in budding yeast, subcellular organelles are more commonly positioned by actin filaments, rather than by microtubules (MTs), we hypothesized that actin filaments connected to the nuclear envelope could be a source of nuclear rotation, which would, in turn, increase α, as shown by our numerical simulations. To test this hypothesis, we fluorescently labeled the SPB, a structure embedded in the nuclear envelope, by tagging Spc29 with Ruby2. Movement of the SPB reflects that of the entire nucleus (Figure 2B). A 1-hr exposure to 25 μm of the sponge toxin Latrunculin A (LatA) was sufficient to completely depolymerize cytoplasmic actin filaments in yeast (Figure S4). By analyzing SPB trajectories, we found that α decreases significantly upon LatA treatment, from $\alpha^{DMSO} = 0.37 \pm 0.16$ to $\alpha^{LatA} = 0.26 \pm 0.15$ (Figure 2B), suggesting that actin filaments indeed contribute to nuclear rotation/precession. The values for k_c, D_c, and L_c were not significantly reduced after LatA treatment (Figures 2B and S3A). A simple explanation for this phenomenon could be that the nucleus rocks back and forth in the x and y planes, with only the frequency of this motion being reduced by LatA. In this case, the total area scanned by the SPB remains the same, while α, which characterizes its motion, decreases upon actin depolymerization. The fact the second dynamical parameter (D_c) does not change suggests that the frequency of the nuclear precession is large compared to the imaging time step (80 ms). Indeed, given that α is a dynamic parameter computed over the first six time points, it incorporates motion up to 0.48 s. This is illustrated in Figure 2A, where the gap between the curves is larger at longer times.

To see whether nuclear oscillation is necessary for the dynamic changes in chromatin following induction of a DSB, we tracked DSB mobility after treatment with LatA. As observed for the SPB, LatA treatment reduces Lc in the uncut condition ($L_c^{uncut\ No\ drug\ 80ms} = 0.13 \pm 0.03$ μm to $L_c^{uncut\ LatA\ 80ms} = 0.08 \pm 0.03$ μm). Upon cleavage, however, this value increases to $L_c^{cut\ LatA\ 80ms} = 0.15 \pm 0.06$ μm, showing approximately the same fold increase as we observed at a break without LatA (Figure 2C). Thus, the DSB-induced increase in movement is not a result of actin filament-driven dynamics. The spring constant k_c follows the same trend upon LatA exposure (Figure S5B). In other words, tethering forces are released following break induction even in the presence of LatA. Interestingly, the diffusion coefficient of the DSB does not change upon LatA treatment, which we attribute to the timescale of the nuclear oscillations, as explained in the previous paragraph.

We note that the anomalous exponent α decreases strongly upon LatA treatment ($\alpha^{uncut\ No\ drug\ 80ms} = 0.48 \pm 0.14$ to $\alpha^{uncut\ LatA\ 80ms} = 0.30 \pm 0.14$), consistent with the suggestion that actin polymerization indirectly influences the underlying nature of chromatin movement (Spichal et al., 2016). Importantly, however, α again increases strongly from $\alpha^{uncut\ LatA\ 80ms} = 0.30 \pm 0.14$ to $\alpha^{cut\ LatA\ 80ms} = 0.46 \pm 0.14$, upon induction of a DSB, despite the presence of LatA (Figure 2D). The same highly significant change was observed for trajectories taken at $\Delta t = 300$ ms (Figure S5C). Thus, the change in locus dynamics at a DSB is not actin-filament dependent, even though basal chromatin movement is influenced by actin-driven nuclear rotation. Importantly, we show that changes in α can be masked by such oscillations.

Effect of Microtubule Depolymerization on Chromatin Dynamics

Early work had shown that MT depolymerization by Nocodazole in yeast increased chromatin dynamics (Marshall et al., 1997), as it releases centromeres from their attachment to the SPB (Bystricky et al., 2004). In contrast, recent work in a mammalian system showed the opposite effect: MT depolymerization

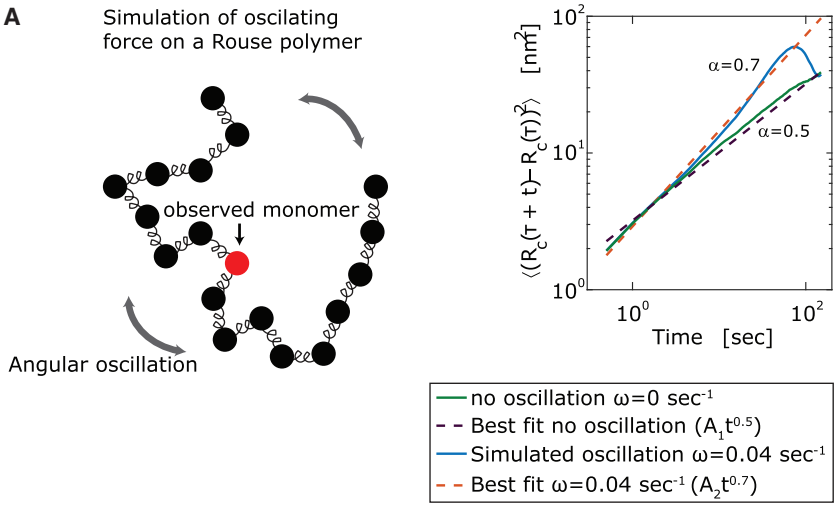

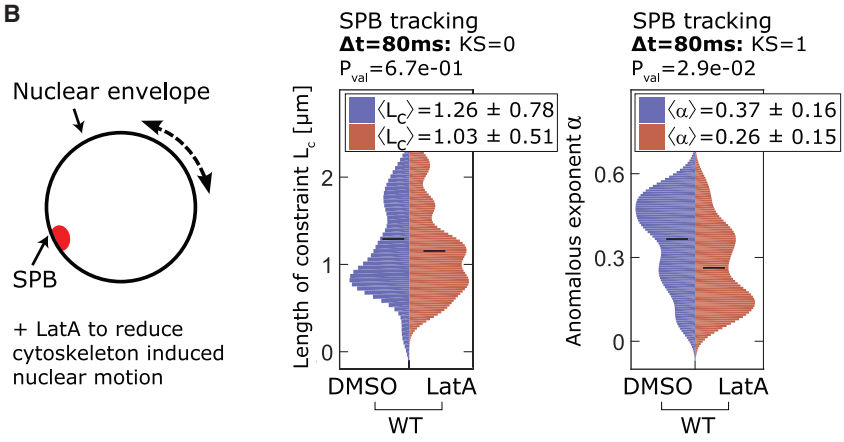

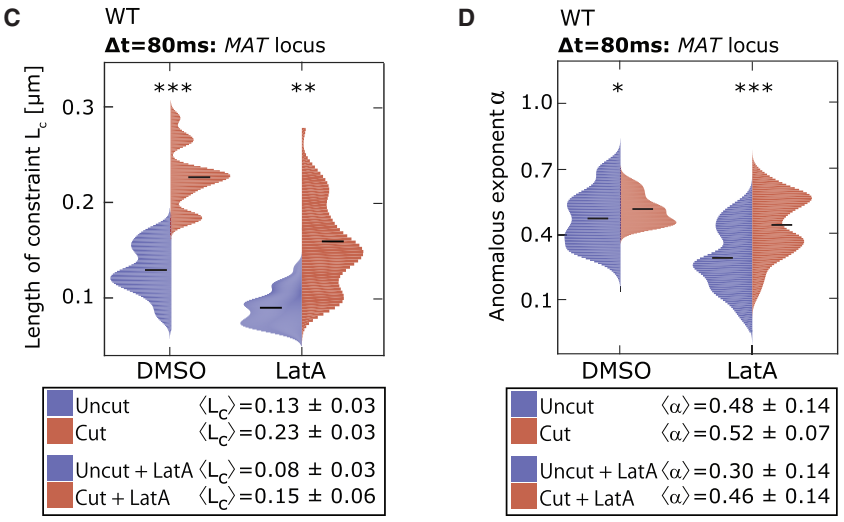

Figure 2. Depolymerization of the Actin Cytoskeleton Reduces Nuclear Rotation but Does Not Prevent DSB-Induced Movement

(A) The effect of rotation on the anomalous exponent α of a monomer within a Rouse polymer. When an angular velocity of ω = 0.04 s^{-1} is applied to the polymer, α increases from 0.5 (Rouse polymer) to 0.7.

(B) The spindle pole body (SPB) is embedded in the nuclear membrane and is visualized by Spc29-Ruby2. Its movement is used to monitor nuclear rotation/precession. Plots show α and Lc of the SPB after 1-hr treatment with the solvent DMSO or 25 μM LatA, which fully depolymerizes actin cables (Figure S4). Strain used is GA-9045.

(C and D) The Lc (C) and α (D) for *MAT*, derived from trajectories taken at Δt = 80 ms ± 25 μM LatA before and after 2 hr DSB induction (for strains, see Figure 1). Corresponding k_c and D_c values, as well as all values for Δt = 300 ms, are in Figure S5. Cut efficiencies are in Table S2.

*p ≤ 0.05, **p ≤ 0.01, ***p ≤ 0.001, respectively. See related Figures S3–S5.

decreased uncapped telomere movement (Lottersberger et al., 2015). Therefore, we revisited this question in yeast to access how MT depolymerization affects chromatin movement. We exposed yeast cells to 50 μM Nocodazole for 1 hr, which is sufficient to arrest cells in G2/M phase due to activation of the spindle assembly checkpoint, and subjected the *lacO*-tagged *MAT* locus to time-lapse imaging, in the presence and absence of a DSB. Interestingly, MT depolymerization (in contrast to actin depolymerization) increased both L_C and α and reduced tethering forces (k_c) at Δt = 80 ms (Figure 3). Following DSB induction, however, there was no further change in movement, with the exception of a marginal decrease in L_C and increase in k_c. Thus, MT depolymerization appears to increase chromatin movement to such an extent that a further increase due to local chromatin changes is not detectable. We attribute the increased chromatin dynamics upon Nocodazole treatment to the depolymerization of the MTs that tether yeast centromeres to the SPB. In mammals, this effect would not be observed since there are no direct MT connections from centrosome to kinetochore in interphase cells. Rather, it was proposed that the effect of Nocodazole in mammalian cells, i.e., the loss of increased chromatin movement after DNA damage (Lottersberger et al., 2015), stems from the loss of the link between cytoplasmic MT and either the nucleoskeleton or chromatin through the LINC complex (Linker of Nucleoskeleton and Cytoskeleton, (Tapley and Starr, 2013)), thus being more similar to the effects of LatA in yeast. Complicating this interpretation is

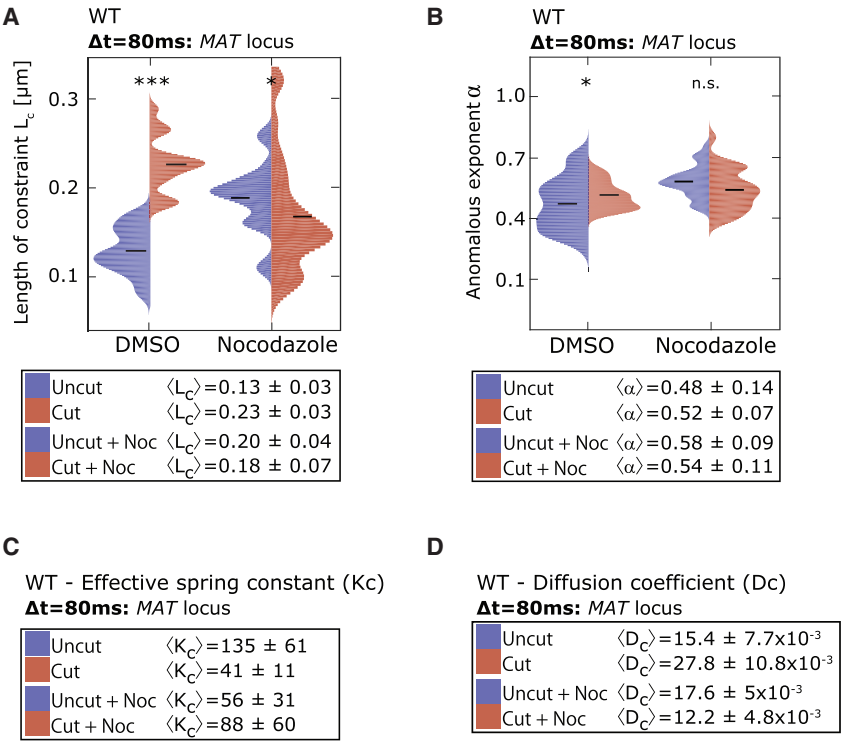

Figure 3. Nocodazole Increases Chromatin Mobility, and There Is No Further Increase after Break Induction

(A–D) The Lc (A) and α (B) values for *MAT*, derived from trajectories taken at $\Delta t = 80$ ms before and after 2 hr DSB induction are given. Strains are as in Figure 1. Where indicated, 50 μM Nocodazole was added for the last hour of HO induction. Corresponding k_c (C) and D_c (D) values are calculated from the same dataset. Cut efficiencies are in Table S2. *$p \leq 0.05$ and ***$p \leq 0.001$.

the fact that Nocodazole may induce cohesin cleavage in HeLa cells (Nakajima et al., 2007), an event that increases chromatin movement in yeast (Dion et al., 2013).

In summary, chromatin dynamics in yeast and mammalian cells showed opposite effects of MT depolymerization: in yeast, MTs can constrain chromatin movement, while actin filaments drive nuclear rotation. Removal of nuclear rotation/precession by LatA created conditions under which changes in SPT parameters were more apparent, while centromere release in yeast seemed to mask enhanced DSB mobility. In contrast, using MSD analysis in mammalian cells cytoplasmic MTs and dynein appeared to drive chromatin movement, an effect that was enhanced during the DNA damage response (Lottersberger et al., 2015). Actin depolymerization had no reported effect.

A Polymer Model Predicts Chromatin Expansion at a DSB

Post-translational modifications on histones and repair/signaling proteins recruited to DSBs are extensive and occur rapidly at DSBs. These include histone acetylation, ubiquitination, and phosphorylation, as well as histone variant exchange and nucleosome eviction by nucleosome remodelers (Smeenk and van Attikum, 2013). Given the large change in α at the site of a DSB once nuclear oscillations were removed ($\alpha^{uncut\ LatA} = 0.30$ to $\alpha^{cut\ LatA} = 0.46$), we next explored the consequence of this change on chromatin structure, using a generalized polymer model called the β-polymer model (Amitai and Holcman, 2013b). This model allows for local interactions between monomers to be calculated from a given anomalous exponent by the relationship $\alpha = 1 - 1/\beta$ (see Supplemental Information). In other words, this polymer model allows us to explore the effects of a changing anomalous exponent on the local organization of the polymer (Figure 4A). This β-polymer model can be used when anomalous exponents are in the range of $\alpha = 0$–0.5, giving us an advantage over other polymer models, such as the Rouse model in which α must be 0.5. Importantly, while other polymer models can predict anomalous exponents for a chromatin locus with values smaller than 0.5 (Weber et al., 2010), none of them can interpret changes in α of the kind we observe following DNA damage.

To mimic the locus mobility before and after DSB induction, we constructed polymer models with anomalous exponents that were extracted from actual trajectories (Figure 4B). We found that as α increases there is a subsequent decompaction of the polymer (Figure 4B). This is quantified by an increase in the radius of gyration Rg, which is the mean distance of the monomers to the center of mass, from 1.21*b* when $\alpha = 0.33$, to 2.34*b* when $\alpha = 0.5$ (here b is distance between two adjacent monomers, for further details see Supplemental Information). Therefore, higher α values are associated with a more open chromatin state. This model thus predicts that chromatin will expand following induction of a DSB (Figure 4B).

To test this prediction, we measured the volumes occupied by the 10 kb of *lacO* array-containing chromatin near the DSB, using 3D super-resolution structured illumination microscopy of GFP-lacI fluorescence (3D-SIM, with an estimated resolution of ~120 nm xy and ~350 nm z; Figure 4C). We quantified the spot volume for hundreds of cells (250–1,030 foci per sample) with and without HO induction. We found that the 3D spot volume increased significantly upon cut induction in S-phase cells, from $V^{uncut} = 0.090 \pm 0.041\ \mu m^3$ to $V^{cut} = 0.109 \pm 0.086\ \mu m^3$ (Figure 4C; Table S4). This striking increase (+20%) confirms the prediction of the β-polymer model and corresponds to an increase in α from 0.33 to 0.45.

Nucleosome Remodeler INO80 Drives Increased α Independent of Actin Dynamics

If decompaction is truly a reflection of altered nucleosome packing, then we should be able to modulate it by eliminating the recruitment of the INO80 remodeler, which is recruited to damage in an Arp8-dependent manner. Loss of INO80 recruitment reduces nucleosome eviction at DSBs and attenuates the

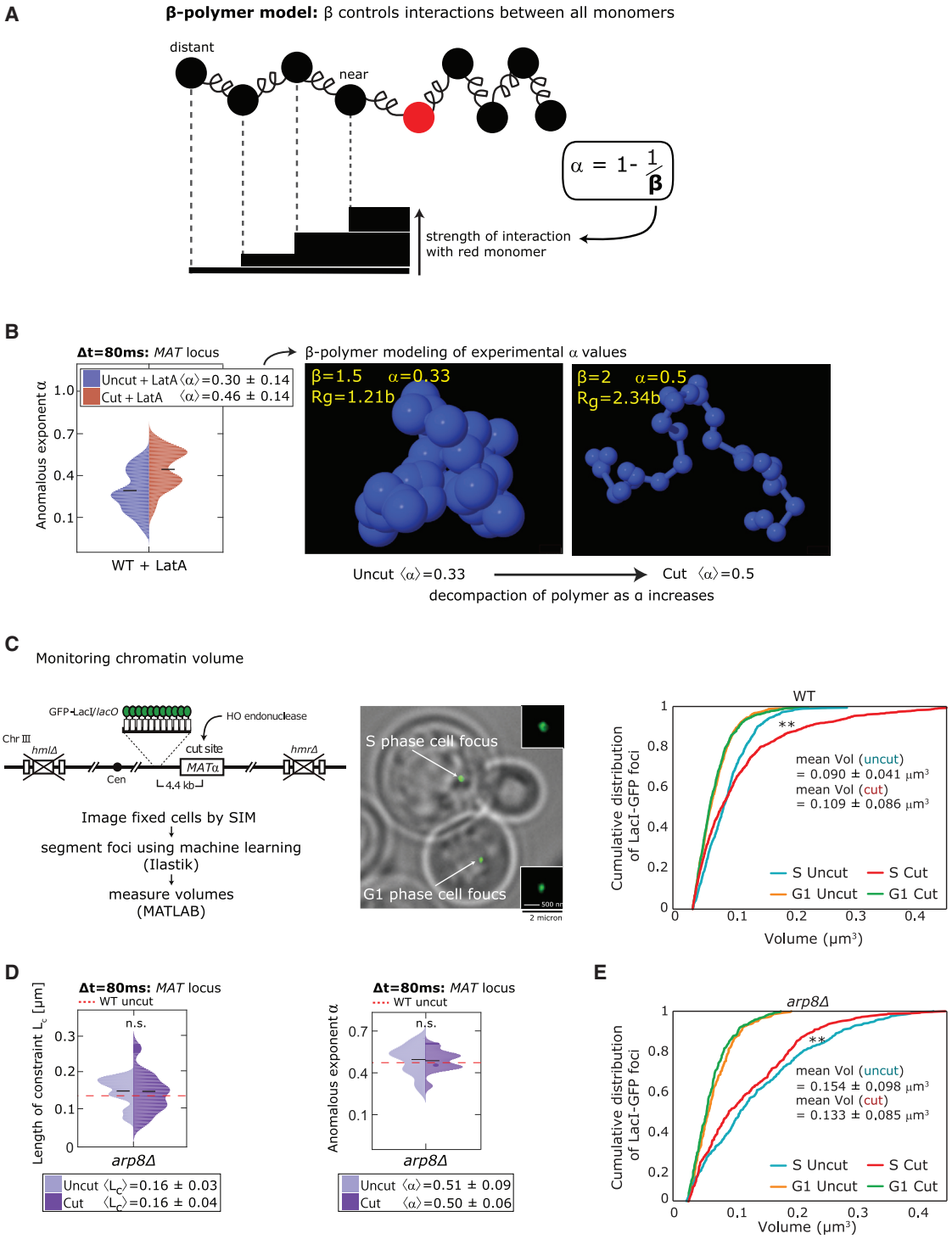

Figure 4. Polymer Simulations Predict Chromatin Expansion at a DSB, which Is Confirmed Experimentally with Structured Illumination Microscopy

(A) The β-polymer model allows for the interactions between all monomers to be controlled and measured in simulations. The strength of interaction of all monomers with any other monomer decays with distance. Anomalous diffusion α is related to β by $\alpha = 1-1/\beta$.

(B) β-polymers where the inter-monomer interactions are modified, with β values corresponding to α values obtained from biological experiments ($\beta = 1.5$ gives $\alpha = 0.33$, and $\beta = 2$ gives $\alpha = 0.5$). The radius of gyration Rg (yellow) measures the degree of compaction. Balls (blue) represent the monomers of radius 0.3*b*.

(C) Experimental system used to acquire and analyze SIM images of the *MAT* locus (left), and an example image showing a G1- and S-phase focus (middle), cumulative distribution function of the 3D volume of spots ± cleavage in wild-type (WT), strain GA-8067 (right). Cells were synchronized with α-factor to obtain G1

(legend continued on next page)

enhanced chromatin dynamics provoked by a DSB (Neumann et al., 2012; Seeber et al., 2013; Strecker et al., 2016). Arp8 is an integral component of the INO80 remodeler that is required for its nucleosome remodeling activity (van Attikum et al., 2007). Interestingly, cells lacking Arp8 have strong recombination defects (Agmon et al., 2013; Strecker et al., 2016) but only mild defects in checkpoint activation or resection (Chen et al., 2012; van Attikum et al., 2007). With this in mind, we tracked locus mobility in an *arp8Δ* strain, before and after DSB induction. Confirming previous reports (Neumann et al., 2012; Strecker et al., 2016), we find that Arp8 is required for increased mobility at the DSB: neither the *Lc*, α, *Dc*, nor k_c changed after cut induction (Figures 4D and S6).

Based on our interpretation of α as an indirect indicator of condensation state (Figure 4A), we monitored locus volume using super-resolution microscopy in the *arp8Δ* strain. The DSB and its surrounding chromatin not only failed to increase spot volume in the absence of Arp8, but volumes were slightly reduced (Figure 4E). This links chromatin expansion at the break to the remodeling activity of INO80 and suggests that INO80 may function at breaks to open chromatin facilitating recruitment of repair proteins (van Attikum et al., 2007).

Increasing α at a DSB Can Provoke Extrusion of Damage from a Chromatin Domain

Our data argue that chromatin expands at a DSB, presumably resulting from a reduction in local forces between monomers (nucleosomes) near the break. Experimentally, we know that DSBs trigger changes in chromatin organization and that they can move from one nuclear sub-compartment to another (Chiolo et al., 2011; Horigome et al., 2014; Jakob et al., 2011; Ryu et al., 2015; Torres-Rosell et al., 2007), yet it is not known how these are related, i.e., whether changes in chromatin at the site of a break affect the long-range architecture of a chromatin domain or a chromosome. Here, we used numerical simulations to ask what happens to the overall structure of a polymer if we reduce the intrinsic interactions of a single monomer, i.e., of a nucleosome near a DSB. The simulations further allow us to modulate the strength of interactions between all monomers, enabling us to test a range of situations that involve changes in specific inter-nucleosomal interactions, mimicking a controlled spread of decondensation from the site of damage.

To account for changes in the chromatin structure and to avoid interpenetration of the chromosome, we added repulsion interactions between each monomer (i.e., Lennard-Jones or LJ interactions) to the β-polymer model (see Figure S7 and Table S3). We considered a polymer of length n = 33, with a coefficient β = 1.5, where all monomers are highly connected (Figure 5A). We note that with the addition of LJ-interaction forces, the relationship between the exponent of the model and the measured anomalous exponent $\alpha = 1 - 1/\beta$, no longer holds, and the numerically estimated α for a self-avoiding polymer with β = 1.5 for a given monomer is α = 0.52.

We then simulated the effect of a DSB on chromatin organization by reducing interactions of the middle monomer n = *17* (red monomer), such that longer-range connections are lost, and only nearest neighbor contacts remain (green monomers, Figure 5B). Surprisingly, this modification had a dramatic effect on the global structure of the polymer with the middle monomer being extruded to the periphery of the globular chromatin domain (Figure 5B). If we mimic the spreading of decondensation by removal of local forces acting on the two neighbors of the middle monomer (n = 16, 18), the effect is even more pronounced (Figure 5C). In analogy to the documented behavior of a DSB in heterochromatin, we find that the more condensed the polymer is, the more pronounced the extrusion effect will be. Moreover, the extrusion is stable as long as the reduced interactions persist: once shifted, the extruded monomer stays at the periphery of the chromatin domain (Figure S8).

We next simulated the effect of extrusion on movement by following the displacement of either an unmodified monomer (n = 10) or the break-mimicking modified monomer (n = 17) (Figure 5D). While the unmodified monomer does not change its position significantly, the modified monomer is highly mobile. To quantify this effect, we plot the average distance of each monomer from the center of mass (cm) of the polymer (Figure 5E). Before extrusion, the middle monomer was closest to the cm (see Figure 5A), but as forces are reduced on this monomer it moves further away (Figure 5E). Finally, we analyzed α for each monomer during the extrusion process. We find that when the interactions are removed from the middle and two neighbor monomers (Figure 5C), α increases sharply from 0.52 to 0.88 (Figure 5F). This is consistent with our empirical observations of increased α upon DSB induction and local chromatin expansion at the break. This polymer modeling suggests that expansion at the site of the break, reflected as increased α, is sufficient to shift a DSB to the periphery of its local chromatin domain.

Previous work has shown that DSBs that occur in heterochromatin or in the nucleolus must move out of these domains to be repaired by the recombination machinery (Chiolo et al., 2011; Ryu et al., 2015; Torres-Rosell et al., 2007; Tsouroula et al., 2016). To see whether this extrusion correlates with reduced forces at the break (i.e., increased α), we monitored the dynamics of an inducible I-SceI cut site integrated into the yeast rDNA with an adjacent *tetO* array, which is visualized by expressing TetR-mRFP (Torres-Rosell et al., 2007). The yeast strain further expressed a YFP-tagged Rad52, which is largely excluded from the nucleolus, and a plasmid-borne galactose-inducible I-SceI endonuclease, as well as constitutively expressed Nucleolar protein 1 (NOP1)-CFP. Rad52-YFP only co-localizes with the TetR-mRFP array when the locus has been extruded from the nucleolus (Figure 5G). To create the break, we induced I-SceI for 2 hr. To avoid interference by nuclear

cells, and S-phase cells were collected 30 min after release from pheromone. Cut induction was 30 min (see Supplemental Information). **p $\leq$ 0.01. For foci counted, cut efficiencies, and statistics, see Tables S2 and S4.

(D) The parameters Lc and α derived from Δt = 80 ms imaging regimen in *arp8Δ* after 2-hr HO induction (strains GA-8921//8922). Cut efficiencies are in Table S2.

(E) Spot volumes as in (C) but for *arp8Δ* (GA-9602). See also Figures S6 and S8.

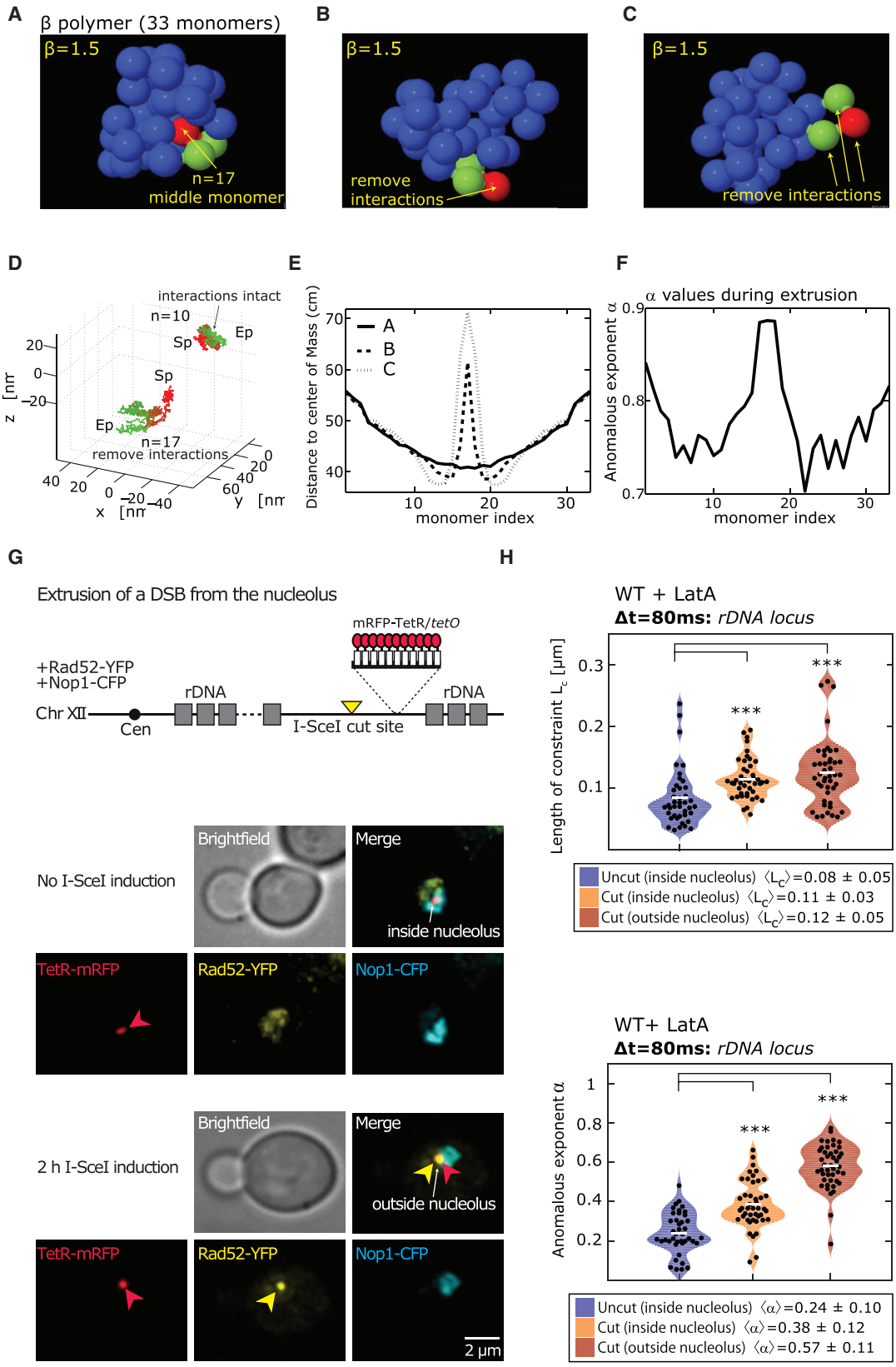

(legend on next page)

oscillation, we included 25 μm LatA during the last hour of cut induction. Dual acquisition (Δt = 80 ms) of TetR-mRFP and Rad52-YFP signals was performed in S-phase cells, where we track three conditions: first, an uncut locus (found within the nucleolus), second, a cut locus (I-SceI is expressed but the array remains within the nucleolus and no Rad52-YFP is bound), and, third, the cut locus that is relocated outside the nucleolus and bound by Rad52-YFP. We find that after break induction *Lc* increases from L_c^{uncut} = 0.08 ± 0.05 μm to $L_c^{cut(inside)}$ = 0.11 ± 0.03 μm and $L_c^{cut(outside)}$ = 0.12 ± 0.05 μm (Figure 5H). Importantly, we find that α increases very strongly both upon cleavage and again upon relocation from the nucleolus (α^{uncut} = 0.24 ± 0.1 μm to $\alpha^{cut(inside)}$ = 0.38 ± 0.12 μm and $\alpha^{cut(outside)}$ = 0.57 ± 0.11 μm). This increase in α likely reflects changes in the contacts at the site of break, further supported by the decrease k_c (Figure S9). It suggests that chromatin surrounding a break, extruded from the nucleolus, is more decondensed than a break within the nucleolus, consistent with a requirement for relocation for Rad52 binding (Torres-Rosell et al., 2007).

Intriguingly, in the absence of LatA the L_C shows the opposite trend: the uncut locus was more dynamic than the cut one (Figure S9). While surprising, we note that the rDNA is segregated from the rest of the nucleus and is attached to the inner nuclear membrane opposite of the SPB by an inner nuclear membrane complex called CLIP (Mekhail and Moazed, 2010) (Figure 6). We hypothesize that the nucleolus is subject to the effects of nuclear precession more than internal loci, and thus an uncut rDNA locus, which is more tightly linked to the nuclear envelope, may be more influenced by cytoskeletal dynamics. After DSB induction, the shift of the locus to the nucleoplasm should reduce nuclear envelope association and Lc or the length of its trajectory within a given time frame may be reduced. Regardless of trajectory length, we found that α increases from α^{uncut} = 0.38 ± 0.06 μm to $\alpha^{cut(outside)}$ = 0.53 ± 0.16 μm, both in the presence and absence of LatA.

Our experimental data thus recapitulate the predicted behavior of the β-polymer model of chromatin surrounding a DSB. The reduction of contacts at the site of a break, observed as domain expansion or an increase in α, reflect a local change in chromatin architecture that allows extrusion to occur. Notably, once chromatin at a DSB has acquired these characteristics, either through the actions of chromatin remodelers such as INO80 (Neumann et al., 2012), or by ubiquitination or SUMOylation of break associated nucleosomes (Horigome et al., 2016; Ryu et al., 2015; Torres-Rosell et al., 2007), break extrusion could occur without a requirement for active translocation. While we do not exclude that directed motion might also occur, the increase in α that leads to extrusion could simply result from reorganization to a minimal energy configuration of the polymer. This biological mechanism may also play a role in other processes that require locus repositioning, for instance, during transcriptional activation.

DISCUSSION

Polymer modeling is a powerful tool to analyze changes in chromatin structure. The choice of polymer model that best recapitulates the behavior of chromatin is open and highly debated. Here, we make the case for a family of polymer models called the β-polymer (Amitai and Holcman, 2013b), as it has the advantage of being able to account for changes in locus dynamics when movement is characterized by variable values for the anomalous exponent α. In addition, we show here that image sampling rate and external forces acting on the nucleus, such as actin filament-driven nuclear oscillation, can strongly affect the results obtained from SPT analysis. These can obscure the underlying properties of chromatin motion and must be taken in to account in live cell chromatin dynamics.

Previous studies of chromatin locus dynamics have relied largely on MSD analysis, which monitors the volume of sampled nuclear space, without shedding light on the nature of the forces acting on the locus in question (reviewed in Dion and Gasser, 2013). In contrast, the analysis workflow presented here dissects the velocity of a locus into external forces acting on the chromatin fiber and internal interactions along the chromatin fiber. The four parameters we extract (α, Lc, Kc, and Dc) contain different information and are largely independent of each other (described in Figures S10A and S10B). By incorporating these experimentally extracted values into polymer models we have predicted that chromatin will decompact at a DSB and that this should lead to the extrusion of the damage from its local chromatin domain. We confirmed both these predictions in yeast by live imaging of an inducible site-specific DSB, either at *MAT* or in the rDNA array. Consistently, an earlier study modeled human Chr 11 using the expression-dependent Dynamic Loop Model (Zhang and Heermann, 2014), in which loops create

Figure 5. Predicted Monomer Extrusion to the Periphery of Its Local Domain upon Loss of Forces between Monomers, and Confirmation with an rDNA DSB

(A) Steady-state configuration of a β-polymer model (β = 1.5 and n = 33 with Lennard-Jones interactions) where the middle monomer (n = 17) is colored in red and its neighbors (n = 16, 18) in green.

(B and C) (B) Modeling predicts this outcome upon removing inter-monomer interactions in a β-polymer at n = 17 and (C) at n = 16, 17, 18.

(D) Two trajectories following a monomer unaffected by the extrusion (n = 10) and the middle monomer (n = 17) (forces removed as in C). At time t = 0 (S_p initial point, in red), the interactions for monomers n = 16, 17, 18 are instantaneously removed. Over 0.05 s, the color changes gradually to green until the end point E_p.

(E) Average distance of each monomer from the center of mass corresponding to (A) full line, (B) dashed line, and (C) dotted line.

(F) The average anomalous exponent α for all different monomers during the extrusion process for case (C).

(G) Strain schematic (GA-6587) showing an I-SceI cut site sequence that has been inserted into the rDNA along with an adjacent *tetO* array, which is visualized by TetR-mRFP binding (red arrows). Cells harbor two plasmids containing either a galactose inducible *I-SCEI* or *NOP1-CFP* (Supplemental Information). When the locus is cleaved by I-SceI and the DSB moves outside the nucleolus, Rad52-YFP can be recruited and forms a focus (red arrows). Rad52 is largely excluded from the nucleolus (Torres-Rosell et al., 2007).

(H) The Lc and α for the strain in (G), derived from trajectories taken at Δt = 80 ms ± 25 μM LatA before and after 2-hr I-SceI induction. LatA was added for the last 1 hr of HO induction. Corresponding k_c and D_c values, as well as values for all parameters in the absence of LatA can be found in Figure S9. ***p ≤ 0.001.

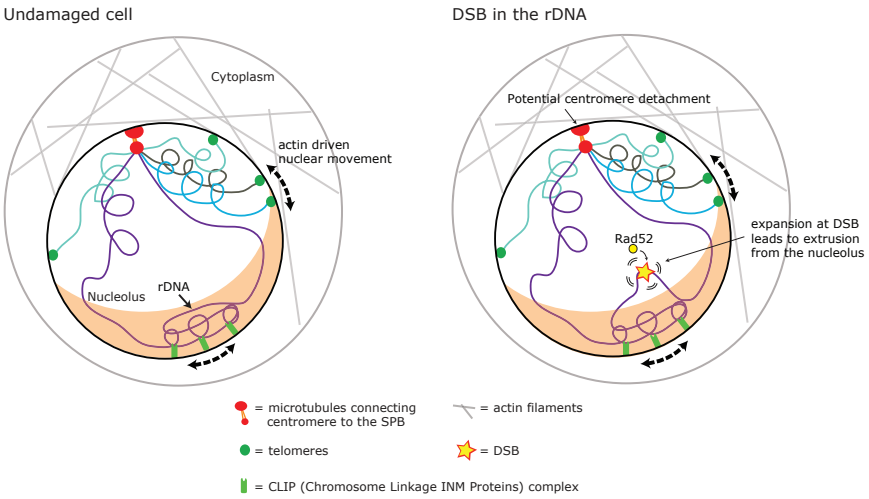

Figure 6. Expansion of Chromatin and Domain Extrusion Provoked by a DSB

Yeast chromosomes are anchored to the nuclear periphery in multiple ways: (1) their centromeres attach to the spindle pole body, (2) telomeres interact through multiple anchors including Sir proteins, SUN domain protein Mps3, Esc1, and Ku, and (3) the CLIP complex can tether the rDNA to the nuclear periphery. Cytoplasmic actin filaments can drive nuclear rotation/precession. After a DSB is induced, local interactions at the break are reduced allowing the chromatin surrounding the break to expand. The loss of interactions leads to the extrusion of the DSB outside of the nucleolus, allowing repair factors like Rad52 to bind.

compartments that are transcriptionally active (fewer loops) or inactive (more loops). By simulation they also found that a break in either an active or inactive domain will shift the site of damage away from the center of mass of the domain. While it was not confirmed experimentally, this is fully consistent with our modeling and experimental results.

Our study does not rule out that loss of an extrinsic tether, such as centromere detachment, could alter chromatin dynamics as reported by others (Strecker et al., 2016). However, our results make it unlikely that such changes are the only driving force behind enhanced break movement. Rather, we argue that the expansion of chromatin at the site of the break due to histone modifications and/or eviction (Smeenk and van Attikum, 2013) enhances α and drives increased movement. While these may be enhanced or altered by events like centromere detachment, in our hands, MT depolymerization and centromere detachment (Bystricky et al., 2004) prior to DSB induction, masks any other increase in mobility. We note that it is crucial for all experimental studies of chromatin dynamics to take into account the effects of nuclear precession, to triage image stacks by cell-cycle stage, and to monitor cleavage efficiency. Without these controls, results are likely to be misleading.

We also present here a quantitative 3D-SIM technique that monitors locus volume, and we show that expansion following a DSB requires the INO80 chromatin remodeling complex. Other remodelers, such as the BAF complex (Swi/Snf or Rsc in yeast) may serve a similar role (Seeber et al., 2014). Importantly, the targeting of INO80 to an uncut locus similarly increases locus dynamics (Neumann et al., 2012), without changing local transcription activity, supporting the notion that the shifting or removal of nucleosomes increases long-range locus dynamics. This has profound implications concerning the impact of local histone modifications on the compaction and spatial behavior of larger chromatin domains. The relevance of our observations is made clear by two recent studies in which a global decompaction of chromatin was observed in response to UV-induced DNA damage in mammalian cells (Adam et al., 2016) and in response to histone degradation in yeast (Hauer et al., 2017). Both studies reinforce and extend the models we simulated here.

As mentioned previously, β-polymer models can only be used when the anomalous exponent is in the range of 0–0.5. This limits their application to constrained, sub-diffusive movement and means that they cannot be used to study directed motion. Nonetheless, most DNA movement has been shown to be subdiffusive (Albert et al., 2013; Amitai et al., 2015; Dion and Gasser, 2013; Weber et al., 2010, 2012). The β-polymer models do not account for possible impact of local heterogeneous crowding on the polymer. On the other hand, by adding other interactions, such as polymer bending or Lennard-Jones forces, we have been able to account accurately for the chromatin dynamics monitored by fluorescent SPTs. We note that movement arising from nuclear rotation/precession leads to an increase in the anomalous exponent α, with or without a DSB. Finally, we show that the problem of additive motion can be circumvented by measuring the dynamics of the locus at different timescales.

New microscopes that allow for 3D imaging without the use of moving stages such as the aberration-corrected multi-focal microscope (Abrahamsson et al., 2013) or a double-helix point spread function microscope (Backlund et al., 2014) will expand the impact of high resolution chromatin locus tracking in the near future, providing even larger datasets that are appropriate for analysis by the β-polymer model presented here.

EXPERIMENTAL PROCEDURES

Yeast Growth Conditions

Yeast strains used in this study are in Table S1. Yeast cultures were grown 30°C, and imaging was performed at 25°C. Strains were either W303 background or JKM179, as described in Table S1. The Ruby2 fluorophore plasmid was acquired from Lee et al. (2013). For DSB live-tracking experiments, yeast were grown at 30°C on YPAD prior to dilution into synthetic media containing 3% glycerol and 2% lactate (SCLG) for several generations prior to the addition of 2% galactose to induce expression of HO. Unless otherwise indicated, 2-hr induction of HO was used, and the efficiency of endonuclease cleavage at *MAT* was determined by quantitative PCR with TaqMan probes as previously described, and qPCR values were normalized to the SMC2 locus (van Attikum et al., 2007). Cutting efficiencies are summarized in Table S2. See Supplemental Experimental Procedures for details.

Microscopy

Live microscopy used a Nikon Eclipse Ti microscope, two EM-CCD Cascade II (Photometrics) cameras, an ASI MS-2000 Z-piezo stage, and a PlanApo ×100,

numerical aperture (NA) 1.45 total internal reflection fluorescence microscope oil objective and Visiview software. Fluorophores were excited at 561 (Ruby2, mCherry), 515 (YFP), and 491 (GFP) nm. GFP and mCherry/Ruby2 fluorescence were acquired simultaneously on separate cameras. A Semrock FF01-617/73-25 filter was used to capture the mCherry/Ruby2 signal on camera 1, and a Semrock FF02-525/40-25 filter was used to capture the GFP signal on camera 2. Time-lapse series were conducted taking eight optical slices per stack either every 80 ms for 1 min or 300 ms for 2 min. Each optical slice received either a 10-ms exposure for the 80-ms intervals or 30 ms for the 300-ms intervals. Nuclear volumes are based on an average haploid nuclear radius of 0.9 μm. Time-lapse image stacks were analyzed as in Dion et al. (2012), using a custom-made ImageJ (FIJI) plug-in, to extract coordinates of locus position from the movies. For structured illumination microscopy, and other specifics of staining and foci selection, see Supplemental Experimental Procedures. Spot tracking was carried out with the Fiji plugin Spot Tracker 2D (Neumann et al., 2012).

Extraction of Parameters, Modeling, and Simulations with Rouse Polymer

The extraction of biophysical parameters from the image stacks and their mathematical derivation are described in Supplemental Experimental Procedures. A Rouse polymer is a collection of monomers moving with a random Brownian motion coupled to a spring force originating from the nearest neighbors. We use other polymer models by adding interactions such as bending elasticity, which accounts for the persistence length of the polymer and Lennard-Jones forces (LJ), describing self-avoidance of each monomer pairs. Finally, we used Euler's scheme to generate Brownian simulations. At impenetrable boundary, each rigid monomer is reflected in the normal direction of the tangent plane. See Supplemental Experimental Procedures for details.

Error Propagation and Statistical Significance

Significance between α, Kc, Lc, and Dc values was tested using the non-parametric Kolmogorov-Smirnov (KS) test. p values are either indicated above the figure panels or by asterisks, where *p $\leq$ 0.05, **p $\leq$ 0.01, ***p$\leq$ 0.001, respectively. Error bars on graphs represent the SE unless otherwise stated. LacI-GFP spot size was shown to be normally distributed and then tested for differences using a two-tailed Student's t test (Graph Pad). Significance cut off was $p < 0.05$.

The Polymer Model

To account for the chromatin dynamics, we use the generalized polymer model called the β-polymer model (Amitai and Holcman, 2013b), which accounts for anomalous diffusive behavior with α in the range of 0–0.5, as measured for a yeast in vivo chromatin locus (Hajjoul et al., 2013). We use β-polymer model where all monomers are connected through a quadratic potential defined by

$$U_\beta(\boldsymbol{R}_1,..\boldsymbol{R}_N,\beta)=\frac{1}{2}\sum_{l,m}A_{lm}\boldsymbol{R}_l\boldsymbol{R}_m,$$

with coefficients

$$A_{l,m}=\sum_{p=1}^{N-1}\tilde{\kappa}_p\alpha_p^l\alpha_p^m=4\kappa\frac{2}{N}\sum_{p=1}^{N-1}sin^\beta\frac{p\pi}{2N}\cos\left(\left(\mathrm{l}-\frac{1}{2}\right)\frac{p\pi}{N}\right)\ \cos\left(\left(\mathrm{m}-\frac{1}{2}\right)\frac{p\pi}{N}\right)$$

and

$$\tilde{\kappa}_p=4\kappa\overset{\beta}{\sin}\left(\frac{p\pi}{2N}\right)\ \text{ for }\ p=0..N-1.$$

In such a model, the strength of interaction $A_{l,m}$ decays with the distance $|l-m|$ along the chain. By definition, $1<\beta<2$ (Amitai and Holcman, 2013b) and the Rouse polymer is recovered for $\beta=2$, for which only nearest neighbors are connected.

SUPPLEMENTAL INFORMATION

Supplemental Information includes Supplemental Experimental Procedures, ten figures, and four tables and can be found with this article online at http://dx.doi.org/10.1016/j.celrep.2017.01.018.

AUTHOR CONTRIBUTIONS

A.S. and S.M.G. planned experiments and analyzed data. A.S. performed most experiments, and A.A. and D.H. carried out all polymer modeling, theoretical development of the analysis pipeline, and extracted biophysical parameters from imaging data. All four authors wrote the paper.

ACKNOWLEDGMENTS

We thank Luca Giorgetti and Vincent Dion for critically reading this manuscript. We thank Jan Eglinger, Laurent Gelman, and Steve Bourke for imaging support; Michael Lisby for strains; and the Gasser laboratory for exciting discussions. S.M.G. thanks the Swiss National Science Foundation (310030B_156936), the Human Frontier Science Program (RGP-0016), and the Novartis Research Foundation for support.

Received: April 18, 2016
Revised: December 2, 2016
Accepted: January 10, 2017
Published: January 31, 2017

REFERENCES

Abrahamsson, S., Chen, J., Hajj, B., Stallinga, S., Katsov, A.Y., Wisniewski, J., Mizuguchi, G., Soule, P., Mueller, F., Dugast Darzacq, C., et al. (2013). Fast multicolor 3D imaging using aberration-corrected multifocus microscopy. Nat. Methods *10*, 60–63.

Adam, S., Dabin, J., Chevallier, O., Leroy, O., Baldeyron, C., Corpet, A., Lomonte, P., Renaud, O., Almouzni, G., and Polo, S.E. (2016). Real-time tracking of parental histones reveals their contribution to chromatin integrity following DNA damage. Mol. Cell *64*, 65–78.

Agmon, N., Liefshitz, B., Zimmer, C., Fabre, E., and Kupiec, M. (2013). Effect of nuclear architecture on the efficiency of double-strand break repair. Nat. Cell Biol. *15*, 694–699.

Albert, B., Mathon, J., Shukla, A., Saad, H., Normand, C., Léger-Silvestre, I., Villa, D., Kamgoue, A., Mozziconacci, J., Wong, H., et al. (2013). Systematic characterization of the conformation and dynamics of budding yeast chromosome XII. J. Cell Biol. *202*, 201–210.

Amitai, A., and Holcman, D. (2013a). Diffusing polymers in confined microdomains and estimation of chromosomal territory sizes from chromosome capture data. Phys. Rev. Lett. *110*, 248105.

Amitai, A., and Holcman, D. (2013b). Polymer model with long-range interactions: Analysis and applications to the chromatin structure. Phys. Rev. E Stat. Nonlin. Soft Matter Phys. *88*, 052604.

Amitai, A., Toulouze, M., Dubrana, K., and Holcman, D. (2015). Analysis of single locus trajectories for extracting in vivo chromatin tethering interactions. PLoS Comput. Biol. *11*, e1004433.

Aten, J.A., Stap, J., Krawczyk, P.M., van Oven, C.H., Hoebe, R.A., Essers, J., and Kanaar, R. (2004). Dynamics of DNA double-strand breaks revealed by clustering of damaged chromosome domains. Science *303*, 92–95.

Backlund, M.P., Joyner, R., Weis, K., and Moerner, W.E. (2014). Correlations of three-dimensional motion of chromosomal loci in yeast revealed by the double-helix point spread function microscope. Mol. Biol. Cell *25*, 3619–3629.

Bell, A.C., and Felsenfeld, G. (1999). Stopped at the border: Boundaries and insulators. Curr. Opin. Genet. Dev. *9*, 191–198.

Bystricky, K. (2015). Chromosome dynamics and folding in eukaryotes: Insights from live cell microscopy. FEBS Lett. *589* (*20 Pt A*), 3014–3022.

Bystricky, K., Heun, P., Gehlen, L., Langowski, J., and Gasser, S.M. (2004). Long-range compaction and flexibility of interphase chromatin in budding yeast analyzed by high-resolution imaging techniques. Proc. Natl. Acad. Sci. USA *101*, 16495–16500.

Chen, X., Cui, D., Papusha, A., Zhang, X., Chu, C.D., Tang, J., Chen, K., Pan, X., and Ira, G. (2012). The Fun30 nucleosome remodeller promotes resection of DNA double-strand break ends. Nature *489*, 576–580.

Chiolo, I., Minoda, A., Colmenares, S.U., Polyzos, A., Costes, S.V., and Karpen, G.H. (2011). Double-strand breaks in heterochromatin move outside of a dynamic HP1a domain to complete recombinational repair. Cell *144*, 732–744.

Cho, N.W., Dilley, R.L., Lampson, M.A., and Greenberg, R.A. (2014). Interchromosomal homology searches drive directional ALT telomere movement and synapsis. Cell *159*, 108–121.

Chubb, J.R., Boyle, S., Perry, P., and Bickmore, W.A. (2002). Chromatin motion is constrained by association with nuclear compartments in human cells. Curr. Biol. *12*, 439–445.

Chung, D.K., Chan, J.N., Strecker, J., Zhang, W., Ebrahimi-Ardebili, S., Lu, T., Abraham, K.J., Durocher, D., and Mekhail, K. (2015). Perinuclear tethers license telomeric DSBs for a broad kinesin-and NPC-dependent DNA repair process. Nat. Comm. *6*, 7742.

Dillon, N., Trimborn, T., Strouboulis, J., Fraser, P., and Grosveld, F. (1997). The effect of distance on long-range chromatin interactions. Mol. Cell *1*, 131–139.

Dimitrova, N., Chen, Y.C.M., Spector, D.L., and de Lange, T. (2008). 53BP1 promotes non-homologous end joining of telomeres by increasing chromatin mobility. Nature *456*, 524–528.

Dion, V., and Gasser, S.M. (2013). Chromatin movement in the maintenance of genome stability. Cell *152*, 1355–1364.

Dion, V., Kalck, V., Horigome, C., Towbin, B.D., and Gasser, S.M. (2012). Increased mobility of double-strand breaks requires Mec1, Rad9 and the homologous recombination machinery. Nat. Cell Biol. *14*, 502–509.

Dion, V., Kalck, V., Seeber, A., Schleker, T., and Gasser, S.M. (2013). Cohesin and the nucleolus constrain the mobility of spontaneous repair foci. EMBO Rep. *14*, 984–991.

Gartenberg, M.R., Neumann, F.R., Laroche, T., Blaszczyk, M., and Gasser, S.M. (2004). Sir-mediated repression can occur independently of chromosomal and subnuclear contexts. Cell *119*, 955–967.

Hajjoul, H., Mathon, J., Ranchon, H., Goiffon, I., Mozziconacci, J., Albert, B., Carrivain, P., Victor, J.-M., Gadal, O., Bystricky, K., and Bancaud, A. (2013). High-throughput chromatin motion tracking in living yeast reveals the flexibility of the fiber throughout the genome. Genome Res. *23*, 1829–1838.

Hauer, M.H., Seeber, A., Singh, V., Thierry, R., Amitai, A., Eglinger, J., Holcman, D., Owen-Hughes, T., and Gasser, S.M. (2017). Histone degradation in response to DNA damage triggers general chromatin decompaction. Nat. Struct. Mol. Biol. Published online January 9, 2017. http://dx.doi.org/10.1038/nsmb.3347.

Heun, P., Laroche, T., Shimada, K., Furrer, P., and Gasser, S.M. (2001). Chromosome dynamics in the yeast interphase nucleus. Science *294*, 2181–2186.

Horigome, C., Oma, Y., Konishi, T., Schmid, R., Marcomini, I., Hauer, M.H., Dion, V., Harata, M., and Gasser, S.M. (2014). SWR1 and INO80 chromatin remodelers contribute to DNA double-strand break perinuclear anchorage site choice. Mol. Cell *55*, 626–639.

Horigome, C., Bustard, D.E., Marcomini, I., Delgoshaie, N., Tsai-Pflugfelder, M., Cobb, J.A., and Gasser, S.M. (2016). PolySUMOylation by Siz2 and Mms21 triggers relocation of DNA breaks to nuclear pores through the Slx5/Slx8 STUbL. Genes Dev. *30*, 931–945.

Jakob, B., Splinter, J., Durante, M., and Taucher-Scholz, G. (2009). Live cell microscopy analysis of radiation-induced DNA double-strand break motion. Proc. Natl. Acad. Sci. USA *106*, 3172–3177.

Jakob, B., Splinter, J., Conrad, S., Voss, K.O., Zink, D., Durante, M., Löbrich, M., and Taucher-Scholz, G. (2011). DNA double-strand breaks in heterochromatin elicit fast repair protein recruitment, histone H2AX phosphorylation and relocation to euchromatin. Nucleic Acids Res. *39*, 6489–6499.

Kepten, E., Bronshtein, I., and Garini, Y. (2013). Improved estimation of anomalous diffusion exponents in single-particle tracking experiments. Phys. Rev. E Stat. Nonlin. Soft Matter Phys. *87*, 052713.

Krawczyk, P.M., Borovski, T., Stap, J., Cijsouw, T., ten Cate, R., Medema, J.P., Kanaar, R., Franken, N.A.P., and Aten, J.A. (2012). Chromatin mobility is increased at sites of DNA double-strand breaks. J. Cell Sci. *125*, 2127–2133.

Kruhlak, M.J., Celeste, A., Dellaire, G., Fernandez-Capetillo, O., Müller, W.G., McNally, J.G., Bazett-Jones, D.P., and Nussenzweig, A. (2006). Changes in chromatin structure and mobility in living cells at sites of DNA double-strand breaks. J. Cell Biol. *172*, 823–834.

Lee, S., Lim, W.A., and Thorn, K.S. (2013). Improved blue, green, and red fluorescent protein tagging vectors for S. cerevisiae. PLoS ONE *8*, e67902.

Levi, V., Ruan, Q., Plutz, M., Belmont, A.S., and Gratton, E. (2005). Chromatin dynamics in interphase cells revealed by tracking in a two-photon excitation microscope. Biophys. J. *89*, 4275–4285.

Lottersberger, F., Karssemeijer, R.A., Dimitrova, N., and de Lange, T. (2015). 53BP1 and the LINC Complex Promote Microtubule-Dependent DSB Mobility and DNA Repair. Cell *163*, 880–893.

Marshall, W.F. (2002). Order and disorder in the nucleus. Curr. Biol. *12*, R185–R192.

Marshall, W.F., Straight, A., Marko, J.F., Swedlow, J., Dernburg, A., Belmont, A., Murray, A.W., Agard, D.A., and Sedat, J.W. (1997). Interphase chromosomes undergo constrained diffusional motion in living cells. Curr. Biol. *7*, 930–939.

Mekhail, K., and Moazed, D. (2010). The nuclear envelope in genome organization, expression and stability. Nat. Rev. Mol. Cell Biol. *11*, 317–328.

Miné-Hattab, J., and Rothstein, R. (2012). Increased chromosome mobility facilitates homology search during recombination. Nat. Cell Biol. *14*, 510–517.

Nagai, S., Dubrana, K., Tsai-Pflugfelder, M., Davidson, M.B., Roberts, T.M., Brown, G.W., Varela, E., Hediger, F., Gasser, S.M., and Krogan, N.J. (2008). Functional targeting of DNA damage to a nuclear pore-associated SUMO-dependent ubiquitin ligase. Science *322*, 597–602.

Nakajima, M., Kumada, K., Hatakeyama, K., Noda, T., Peters, J.M., and Hirota, T. (2007). The complete removal of cohesin from chromosome arms depends on separase. J. Cell Sci. *120*, 4188–4196.

Nelms, B.E., Maser, R.S., MacKay, J.F., Lagally, M.G., and Petrini, J.H. (1998). In situ visualization of DNA double-strand break repair in human fibroblasts. Science *280*, 590–592.

Neumann, F.R., Dion, V., Gehlen, L.R., Tsai-Pflugfelder, M., Schmid, R., Taddei, A., and Gasser, S.M. (2012). Targeted INO80 enhances subnuclear chromatin movement and ectopic homologous recombination. Genes Dev. *26*, 369–383.

Ptashne, M. (1986). Gene regulation by proteins acting nearby and at a distance. Nature *322*, 697–701.

Roukos, V., Voss, T.C., Schmidt, C.K., Lee, S., Wangsa, D., and Misteli, T. (2013). Spatial dynamics of chromosome translocations in living cells. Science *341*, 660–664.

Ryu, T., Spatola, B., Delabaere, L., Bowlin, K., Hopp, H., Kunitake, R., Karpen, G.H., and Chiolo, I. (2015). Heterochromatic breaks move to the nuclear periphery to continue recombinational repair. Nat. Cell Biol. *17*, 1401–1411.

Seeber, A., Dion, V., and Gasser, S.M. (2013). Checkpoint kinases and the INO80 nucleosome remodeling complex enhance global chromatin mobility in response to DNA damage. Genes Dev. *27*, 1999–2008.

Seeber, A., Dion, V., and Gasser, S.M. (2014). Remodelers move chromatin in response to DNA damage. Cell Cycle *13*, 877–878.

Smeenk, G., and van Attikum, H. (2013). The chromatin response to DNA breaks: Leaving a mark on genome integrity. Annu. Rev. Biochem. *82*, 55–80.

Soutoglou, E., Dorn, J.F., Sengupta, K., Jasin, M., Nussenzweig, A., Ried, T., Danuser, G., and Misteli, T. (2007). Positional stability of single double-strand breaks in mammalian cells. Nat. Cell Biol. *9*, 675–682.

Spichal, M., Brion, A., Herbert, S., Cournac, A., Marbouty, M., Zimmer, C., Koszul, R., and Fabre, E. (2016). Evidence for a dual role of actin in regulating chromosome organization and dynamics in yeast. J. Cell Sci. *129*, 681–692.

Starr, D.A., and Fridolfsson, H.N. (2010). Interactions between nuclei and the cytoskeleton are mediated by SUN-KASH nuclear-envelope bridges. Ann. Rev. Cell Dev. Biol. *26*, 421–424.

Strecker, J., Gupta, G.D., Zhang, W., Bashkurov, M., Landry, M.-C., Pelletier, L., and Durocher, D. (2016). DNA damage signalling targets the kinetochore to promote chromatin mobility. Nat. Cell Biol. *18*, 281–290.

Taddei, A., and Gasser, S.M. (2012). Structure and function in the budding yeast nucleus. Genetics *192*, 107–129.

Tapley, E.C., and Starr, D.A. (2013). Connecting the nucleus to the cytoskeleton by SUN-KASH bridges across the nuclear envelope. Curr. Opin. Cell Biol. *25*, 57–62.

Torres-Rosell, J., Sunjevaric, I., De Piccoli, G., Sacher, M., Eckert-Boulet, N., Reid, R., Jentsch, S., Rothstein, R., Aragón, L., and Lisby, M. (2007). The Smc5-Smc6 complex and SUMO modification of Rad52 regulates recombinational repair at the ribosomal gene locus. Nat. Cell Biol. *9*, 923–931.

Tsouroula, K., Furst, A., Rogier, M., Heyer, V., Maglott-Roth, A., Ferrand, A., Reina-San-Martin, B., and Soutoglou, E. (2016). Temporal and spatial uncoupling of DNA double strand break repair pathways within mammalian heterochromatin. Mol. Cell *63*, 293–305.

van Attikum, H., Fritsch, O., and Gasser, S.M. (2007). Distinct roles for SWR1 and INO80 chromatin remodeling complexes at chromosomal double-strand breaks. EMBO J. *26*, 4113–4125.

Verdaasdonk, J.S., Vasquez, P.A., Barry, R.M., Barry, T., Goodwin, S., Forest, M.G., and Bloom, K. (2013). Centromere tethering confines chromosome domains. Mol. Cell *52*, 819–831.

Weber, S.C., Theriot, J.A., and Spakowitz, A.J. (2010). Subdiffusive motion of a polymer composed of subdiffusive monomers. Phys. Rev. E Stat. Nonlin. Soft Matter Phys. *82*, 011913.

Weber, S.C., Spakowitz, A.J., and Theriot, J.A. (2012). Nonthermal ATP-dependent fluctuations contribute to the in vivo motion of chromosomal loci. Proc. Natl. Acad. Sci. USA *109*, 7338–7343.

Zhang, Y., and Heermann, D.W. (2014). DNA double-strand breaks: Linking gene expression to chromosome morphology and mobility. Chromosoma *123*, 103–115.